HELLENIC CENTRE FOR MARINE RESEARCH

**Mediterranean Marine Science**

VOLUME 15 • Number 4 • (special issue)

**HF Radar observations of the Dardanelles outflow current in North Eastern Aegean using validated WERA HF radar data**

Z. KOKKINI, M. POTIRIS, A. KALAMPOKIS, V. ZERVAKIS

**To cite this article:**

Research Article

# HF Radar observations of the Dardanelles outflow current in the North Eastern Aegean using validated WERA HF radar data

## Z. KOKKINI[1], M. POTIRIS[1], A. KALAMPOKIS[1, 2] and V. ZERVAKIS[1]

[1] Department of Marine Sciences, School of the Environment, University of the Aegean, GR81100, Mytilene, Greece
[2] Dipartimento di Scienze e Tecnologie, Università degli Studi di Napoli "Parthenope", 80143, Naples, Italy.

Corresponding author: mar01045@mar.aegean.gr

Handling Editor: Ioanna Siokou

## Abstract

A two-site WERA High Frequency radar (HF radar) system, named "Dardanos", was installed in November 2009 on the eastern coast of Lemnos Island, North Aegean Sea, to monitor the surface inflow of Black Sea waters exiting from the Dardanelles Strait, as well as to constitute a coastal management tool for incidents of oil-pollution or search-and-rescue operations. Strong interference from external radio signals has been a source of noise deteriorating the quality of the backscattered signal, thus significantly reducing the HF radar's effective operating range. In order to ameliorate this problem, further quality-control and data gap interpolating procedures have been developed and applied, to be used in addition to the procedures incorporated and used by the manufacturer's signal processing software. The second-level processing involves traditional despiking in the temporal domain, preceding Empirical Orthogonal Function analysis. The latter is used not only to filter high-frequency noise but also to fill data gaps in time and space. The data reconstruction procedure has been assessed via comparison of (a) HF radial versus CODE-type drifter radial velocities as well as (b) HF-derived virtual drifter tracks versus actual drifter tracks. The main circulation features and their variability, as revealed by the reconstructed fields, are presented.

**Keywords:** HF radar, drifters, Aegean Sea, surface circulation, Dardanelles, Black Sea Water, DINEOF.

## Introduction

The North Aegean Sea is one of the northern extremities of the Mediterranean, the other two being the Adriatic Sea and the Gulf of Lions. The latter regions are traditionally known as the major dense water formation sites of the Mediterranean Sea (Pollak, 1951; Wüst, 1961). Despite the fact that the North Aegean's potential to be an equally strong formation area as the former sites has been recognized since the earliest oceanographic studies of the Mediterranean (Nielsen, 1912, Plakhin, 1971, 1972); until the 1990s, the Aegean was considered a mere contributor of water to the deep waters of the Eastern Mediterranean (Wüst, 1961; Malanotte-Rizzoli *et al.,* 1997). The Aegean water, being lighter than the Adriatic-originated Eastern Mediterranean Deep Waters (EMDW), upon its passage through the Cretan Straits was reported to lie at a depth of about 1000 m, between the Levantine Intermediate Water (LIW) and the EMDW masses (Miller, 1963; Schlitzer *et al.,* 1991). This thermohaline overturning circulation was considered to be in steady state until the discovery and analysis of the Eastern Mediterranean Transient (EMT) event of the early 1990s, during which the Aegean Sea replaced the Adriatic as the major source of deep water for the Eastern Mediterranean (Roether *et al.,* 1996, 2007). The North Aegean played a

key role in triggering and contributing to this great change (Zervakis *et al.,* 2000; Gertman *et al.,* 2006), thus was been recorded to become a dense-water formation site, as proposed by Nielsen (1912) and Plakhin (1971, 1972). Zervakis *et al*. (2000) attributed the infrequent character of major deep-water formation episodes in the North Aegean to the continuous buoyancy import from the Black Sea through the Dardanelles Strait.

The Black Sea and the Mediterranean are two differently functioning semi-enclosed oceanic basins; the former being a textbook example of a dilution basin, the latter a strong concentration basin (Sverdrup *et al.,* 1947; Tolmazin, 1985). Thus, through their connection via the Turkish Straits System (TSS), comprised of the Straits of Dardanelles and Bosphorus and the interconnecting Sea of Marmara, the two Seas exchange buoyancy in the form of light, low salinity water imported as a surface flow from the Black Sea to the North Aegean, and a subsurface, highly saline layer of Mediterranean water exported from the Mediterranean to the Black Sea (Ünlüata *et al.,* 1990). The continuous inflow of Black-Sea originated water (BSW) into the North Aegean forms a thin (20-40 m) surface layer over the northern parts of this basin, which can control the deep-water formation processes over this region by hindering the exchange of heat and water between the atmosphere

and the subsurface Levantine-originated waters (Zervakis *et al.,* 2000). Thus, the BSW outflow in the North Aegean is critical not only to the upper-layer circulation of the area but also to the thermohaline overturning circulation of the Eastern Mediterranean basins.

The general circulation of the North Aegean is rather well described in the scientific literature (Zodiatis & Balopoulos, 1993; Zodiatis, 1994; Zervakis & Georgopoulos, 2002; Olson, *et al.,* 2007); however, its temporal and spatial variability has not been examined in depth. The complex circulation is due to many factors, such as the geographical distribution of the various islands and coasts, the irregular bottom topography, and the inflow of the relatively low temperature and salinity Black Sea Waters (Poulos *et al.,* 1997). The north-eastern part of the Aegean is dominated by the presence of low salinity Black Sea Water, entering through the Dardanelles Strait (Fig. 1). This cold water occupies the surface layer of the North Aegean and can be easily traced, due to its distinct signature (low salinity and temperature). A large area to the south of the Aegean exit of the Dardanelles Strait is occupied by northward propagating warm and saline water masses entering the Aegean from the eastern Cretan Straights and carrying Levantine Waters (Zodiatis & Balopoulos, 1993; Zodiatis, 1994; Zervakis & Georgopoulos, 2002; Lykousis *et al.,* 2002). The light, brackish (S~28-35) water from the Black Sea enters the North Aegean region due to the surface outflow of the Dardanelles, of volume flux ranging between 200 $km^3 yr^{-1}$ and 1000 $km^3 yr^{-1}$, exhibiting maximum values during spring and summer and minimal values during winter (Ünlüata *et al.,* 1990). This permanent outflow forms a surface layer over the North Aegean, determining the surface layer characteristics (Zervakis & Georgopoulos, 2002; Zodiatis & Balopoulos, 1993; Zodiatis, 1994) and circulation (Tzali *et al.,* 2010), controlling deep-water formation (Zervakis *et al.,* 2000) and fertilizing this area of the Aegean (Lykousis *et al.,* 2002; Siokou-Frangou, *et al.,* 2002). Furthermore, the Dardanelles Strait is considered to be a potential source of marine pollution for the North Aegean due to (a) the great number of merchant vessels and tankers crossing the Turkish Straits, (b) its small width ranging at 4 km with a value of 1.2 km at its narrowest point and (c) its high surface current speeds, reaching as high as 3.5-4 kn. Due to the mean circulation in the area, any oil-spill caused by a potential marine accident in the Dardanelles would enter the North Aegean, with the coasts of Lemnos Island being the most vulnerable to pollutant beaching.

For the above reasons, the University of the Aegean and the Hellenic Center for Marine Research have jointly installed a WERA HF radar (Gürgel *et al*., 1999a), named "Dardanos" along the eastern coast of Lemnos island, for continuous monitoring of the Dardanelles current over the marine region between the islands of Lemnos, Imvros (Gokceada), Lesvos and the Turkish coast (Zervakis *et al.,* 2011) (Fig. 1). This work constitutes a description of the quality control, data reconstruction and assessment procedures followed, and a preliminary analysis of the temporal and spatial characteristics of the surface flows in that region as revealed from the reconstructed data set.
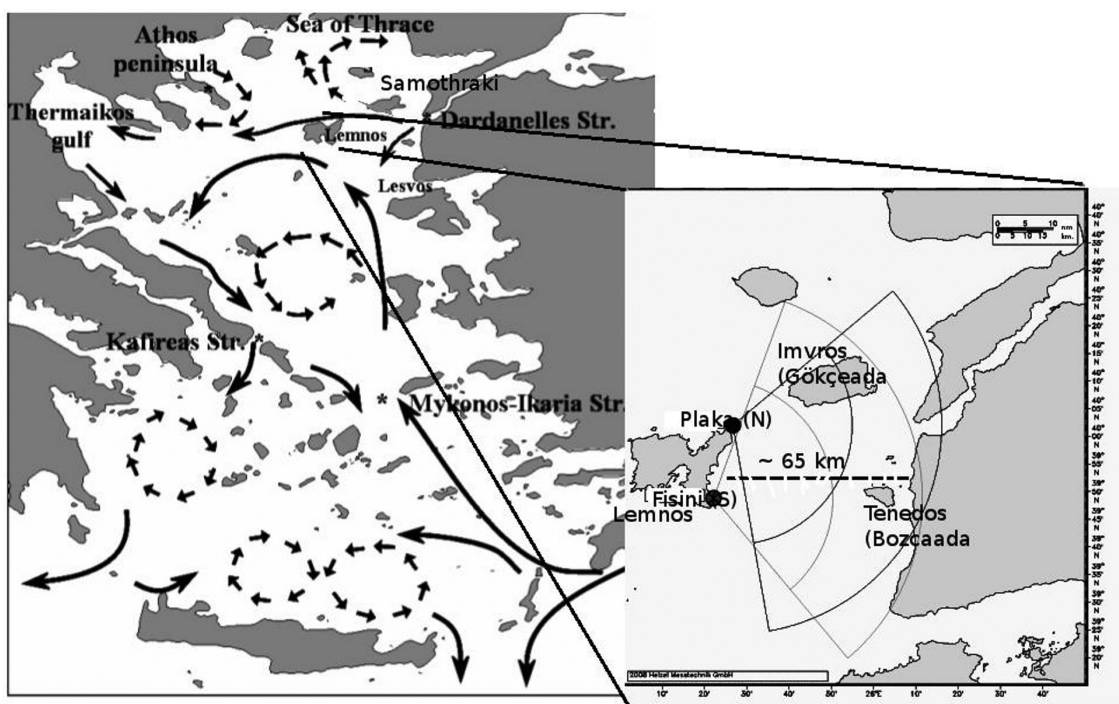


***Fig. 1:*** The study Area. Presentation of the surface circulation and the radar coverage of each site, as is provided by H. Messtechnick. The horizontal distance of the radar coverage area is ~ 65km and the elevations of the two main islands that are inside the area of radar coverage are 12m for Tenedos and 673m for Imvros.

754

*Medit. Mar. Sci., 15/4, 2014, SPECIAL ISSUE, 753-768*

**Materials and Methods**

*The radar data*

The shore-based, high-frequency (HF) radar system was installed within the framework of the INTERREG Archimed project "Prevention and Management of sea-originated Risks to the Coastal Zone (CORI)" on the eastern coast of Lemnos island and is a monostatic four-antenna, dual site HF WEllen RAdar (WERA) (Gürgel *et al.,* 1999b). The installation was completed in October 2009 and two transmit (Tx) and receive (Rx) sites were used, distant by about 23 km from each other: (a) Plaka site, at the North-Eastern Cape and (b) Fisini site, at the South-Eastern Cape of Lemnos Island. Each single station produces a component of the surface current velocity directed toward or away from the radar, hereafter referred to as the radial velocity component. The initial planning required that the system's range extends to the mouth of the Strait, in order to be able to separate the original Dardanelles current from a very energetic anti-cyclone flowing around Samothraki Island, which often contributes to the current flowing through the Lemnos - Imvros Strait (Zervakis & Georgopoulos, 2002; Olson *et al.,* 2007). Thus, the HF radar transmitting frequency was low enough (13.45 MHz) in order to provide a range of 70 km, which is necessary to cover the Dardanelles exit (Fig. 1). In more detail, the Plaka site array was set to transmit at 13.45 MHz and the Fisini site at 13.49 MHz.

Direction finding is used at reception. The Tx bandwidth is 50 kHz and the radial range resolution 3 km. Radial current velocities are obtained for 17.45 min and then a temporal averaging is performed, at a 0.5 hour repetition cycle. The two-dimensional surface current velocity vector is computed by combining the radial velocity components obtained from the two radar stations in the area of signal overlap. The spatial resolution of the HF radar, provided after horizontal interpolation and vector field construction (performed by the WERA software provided) is about 1.5 km; surface circulation maps are provided every half hour. Subsequently, this surface current field can be decomposed into the u (eastward) and v (northward) velocity components.

HF radar algorithms assume that the ocean waves are deep-water wind waves. The deep-water approximation is valid within 0.5%, if the water depth is greater than half of the wavelength (Trujillo *et al.*, 2004). The depth over most of the study area covered by the HF radar exceeds 40 m, except for a small area to the east of cape Plaka, where there is a shallow reef reaching as little as 3 m depth (Fig. 2). Thus, as the Bragg-scattering sea-waves for the 13.45 MHz frequency have a wavelength of 11.1 m, the deep-water dispersion relation is rightfully applied to the vast majority of the domain. All dates and times in this paper refer to a Coordinated Universal Time (UTC).

Preliminary analysis of the data reveals that the system fulfilled the range requirement about 30% of the
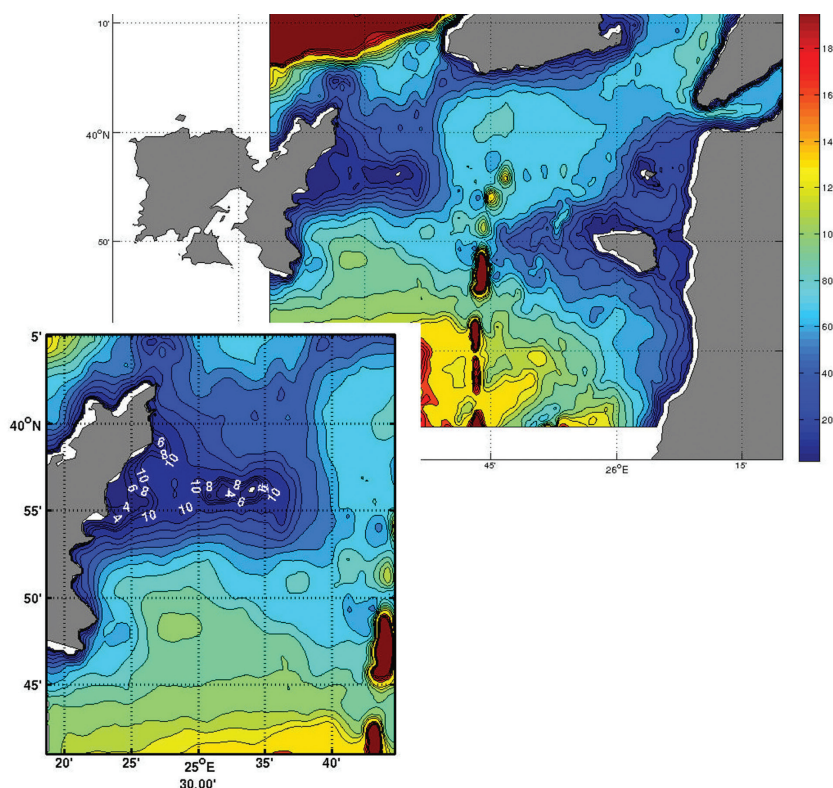


***Fig. 2:*** Bathymetry of the area of interest. (For the first 10 meters depth, the intervals between the contour lines are 2m, from 10m to 100m the interval is 10m and from 100m to 200m is 50m.) The zoomed-in figure presents the contour line of the bathymetry were shallow-water becomes relevant for the radar operation.

time. Temporal variability of spatial coverage is expected in High-Frequency radar systems, due to weather and sea-surface state variability, external radio interference etc. (Gürgel *et al.*, 1999a).

### The drifter data

The drifters used within the radar coverage area were surface CODE-type drifters (Davis, 1985), as modified by the University of the Aegean (Zervakis *et al.*, 2009) and produced by Marine Drifters (www.marinedrifters.eu). Off-the-shelf GPS/GSM modules are used for tracking and communication, with SMS-based fully bidirectional communication capabilities. The drifters were deployed during several expeditions in the same area, in different seasons. The first three expeditions took place within the framework of the MarinERA MedEx project. The first expedition was on 04 December 2009 (MedEx 1), the second on 03 March 2011 (MedEx 3) and the third on 13 May 2011 (MedEx 5). Two longer-lasting expeditions took place in the area within the framework of the MED TOSCA project. The first lasted from 26 May 2012 until 01 June 2012 (Tosca Lemnos 1) and the second from 03 October 2012 until 06 October 2012 (Tosca Lemnos 2). The drifter deployment dates are presented in Table 1.

For the sake of comparison of the HF radar-generated velocity fields with the Lagrangian drifter tracks, virtual drifter tracks were produced through the combination of spatial interpolation on the velocity maps via the nearest neighbour method and position prediction using a $4^{th}$ order Runge-Kutta integrator at the same time-step as the sampling rate of the drifters. The trajectories of the real drifters are compared with the virtual trajectories computed from the radar velocity field.

For every real drifter deployment, a virtual drifter was "deployed" at the same time and position, and its track was estimated based on the method described above.

### Data treatment and second-level quality control of the radar data

Proprietary quality control is already performed on the raw data by the WERA software provided by Helzel Messtechnik. A threshold is set and the outliers are removed from the original data. However, erroneous data still emerge on the WERA-produced radar current maps.

Thus, second-level quality control was developed and applied to the total vector data, before any further analysis was conducted. The second-level processing consists of (a) temporal despiking, meaning the removal of anomalous values based on an empirically determined threshold of 2 times the standard deviations from the running mean of the data time-series, and (b) spatio-temporal filtering and gap-filling via application of the DINEOF method (Alvera-Azcárate *et al.*, 2009, 2011).

The first step of the second-level processing refers to the temporal despiking of the radar semi-hourly data, i.e. identification and removal of anomalous values in the time series of the two current components (u-positive eastward, v-positive northward). Spikes were identified in the time domain, i.e. on the velocity time-series generated in each pixel of the HF radar grid. A subjectively selected temporal window was used to generate running mean and standard deviation estimates along each time series. A spike was defined as a value distant from the running mean more than a subjectively selected multiple of the standard deviation. The process was applied to each grid cell of the radar for the whole period of operation of the radar. The window length that was selected after several trials was 4.5 hours (9 measurements) and the selected threshold for spike definition was equal to 2 standard deviations. This processing removed the vast majority of temporal spikes, but of course, could not eliminate systematic errors. The resulting time series, hereafter referred to as despiked semi-hourly data, constitutes the basis of all subsequent analysis.

### EOFs for data reconstruction

The Empirical Orthogonal Functions (Lorenz, 1956; Kelly, 1988; Emery & Thomson, 2004) method describes the spatial and temporal evolution of geophysical fields, dividing the entire variability into spatial patterns, called modes, and corresponding time-dependent coefficients determining the temporal evolution of the modes, known as expansion coefficients. A scale factor corresponds to each mode and represents the percentage of the total variance explained by this spatial mode. Usually, only a small number of modes explain most of the variability. As the modes are uncorrelated, one can, with the reverse process, reproduce the initial current fields, using only those few modes. The EOF decomposition can be both a valu-

**Table 1.** Drifters deployment dates.

| MedEx experiment | | | Tosca experiment | | |
|---|---|---|---|---|---|
| | | Dates | | | Dates |
| MedEx 1 | 2 CODE drifters | 04/12/2009 | Tosca Lemnos 1 | 4 CODE drifters | 29/05/2012 |
| MedEx 3 | 2 CODE drifters | 11/03/2011 | | 3 CODE drifters | 30/05/2012 |
| MedEx 5 | 2 CODE drifters | 03/05/2011 | | 9 CODE drifters | 31/05/2012 |
| | | | Tosca Lemnos 2 | 5 CODE drifters | 03.10.2012 |
| | | | | 4 CODE drifters | 04/10/2012 |
| | | | | 3 CODE drifters | 05/10/2012 |
| | | | | 4 CODE drifters | 06/10/2012 |

756

*Medit. Mar. Sci., 15/4, 2014, SPECIAL ISSUE, 753-768*

able data-processing tool, enabling noise filtering and the filling of data-gaps (as is used hereafter), and an advanced analysis tool (enabling the determination of the various spatiotemporal modes of responses to forcing).

In this work, EOF decomposition was used primarily as a filtering and interpolation tool. For that purpose, the Data Interpolating EOF (hereafter referred to as DINEOF) method (Alvera-Azcárate *et al.*, 2009, 2011) was implemented in order to complete the missing radar data. The method was applied to the despiked semi-hourly data set described in the previous section. Despite the fact that the data set extends from the end of December 2009 to June 2011, the DINEOF method was not applied to the entire data set due to the high computational cost. In order to preserve the high spatiotemporal variability of the flow in the reconstructed dataset, while keeping the computational cost manageably low, the DINEOF method was applied to successive, partly overlaying parts of the data set, of a record length extending from less than one to two months. The short-length, reconstructed records where then concatenated to create a continuous time series of 1.5 yr. duration and of 0.5 hrs sampling interval, called the "semi-hourly interpolated data".

The DINEOF method is based on the iterative SVD decompositions of an initial data matrix, real or complex valued, initially padded with zeros for missing values and with the results of previous steps thereon. The iteration is repeated until convergence is achieved for each EOF, applied to the dominant EOFs in descending order. In order to decide at which mode to stop the calculation, we used the fact that as the variance explained by each mode becomes progressively smaller, the percentage of pixels whose divergence gets practically infinite increases, due to the gradual reduction of the spatio-temporal scales of the phenomena described by the mode. The exclusion of the high frequency and low energy modes acts as a secondary quality control check that filters out current noisy values. Estimation of the most appropriate number of modes to retain for further analysis is influenced by the spatial and temporal variability of the analyzed fields. In combination with the moving data gaps that have different extensions in different data samples,

one is left with interpolated data of variable goodness of fit values. In order to ensure that no poor quality data were included in the resulting data set used for further analysis, the values of each ensemble that failed to pass a statistical goodness of fit test were rejected.

At the beginning, the DINEOF method was applied to both the despiked data set and the original data set provided by the HF radar. Specifically, the DINEOF analysis was only applied to the total vectors, on a regular vector grid and not on the radial velocities. Furthermore, the complex valued approach was used. The radar coverage area is not constant with time, and erroneous data (spikes) tend to appear near the edges of the instantaneous coverage field. In the long term (more than one month), this results in systematically erroneous velocities beyond the areas where the data return field gradient (e.g. Fig. 3a) is maximum. These current velocities were identified by their anomalously high speeds. Performing DINEOF without the temporal despiking resulted in a "step" of the speed of the interpolated fields where the data return field gradient reached its maximum. This "step" could also be attributed to the lack of energy in the initial field where data return was sparse, as most of the time there were no values and zero padding was performed. While this behaviour was evident in most but not all the ensembles interpolated, working on the despiked data set was the final choice. The resulting eigenvalue spectrum is presented in Figure 4.

### *Performance evaluation*

The evaluation of the performance of the entire system was performed in the following ways:
a) Evaluation of the data reconstruction process by comparing the reconstructed fields with the original data set;
b) Evaluation of the ability of the HF radar to accurately monitor the near surface flow by

 i. Comparison of radial components of the velocities of the drifters along the line-of-sight connecting them to the HF radar antenna sites, with the radial velocity components back-calculated from the reconstructed HF radar data set.
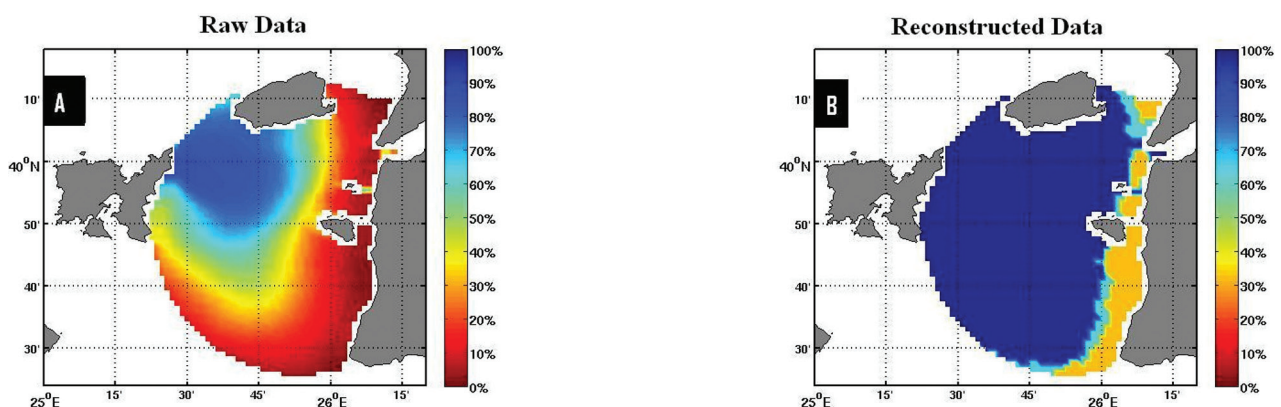


***Fig. 3:*** Data spatiotemporal coverage, for autumn 2010, (a) before the DINEOF application, with a mean coverage around 30% of the total and b) after the DINEOF application, resulting to coverage higher than 70% of the total.
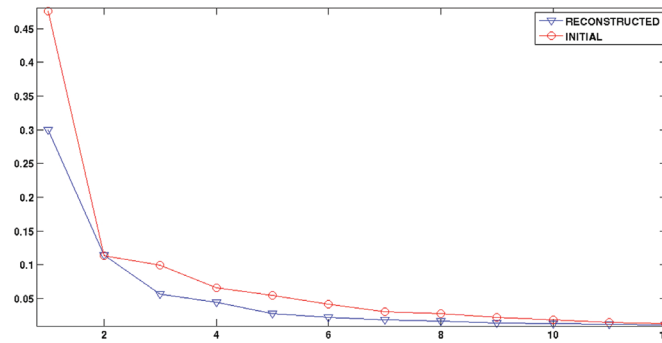
**Fig. 4:** The eigenvalue spectra of an ensemble (January 2010) before and after interpolation.

ii. Comparison of the virtual drifter tracks based on the reconstructed HF-radar velocity fields and actual drifter tracks deployed in the region, and

A more detailed description of the methodology developed for each stage of the evaluation of the performance of the system is presented below:

a) The comparison of the reconstructed current data to the original data set is based on two metrics hereby referred to as space and time Data Reconstruction Errors (DRE). The time DRE, $DU_t$, is defined as the spatially averaged difference between the initial and the reconstructed currents:

$$DU_t(t)= \frac{1}{A}\int\{u_{in}(x,y,t)-u_{rec}(x,y,t)\}dxdy \quad (1)$$

where A is the area over which the integration takes place, $u_{in}(x,y,t)$ and $u_{rec}(x,y,t)$ the original and reconstructed velocity data sets. Similarly to (1), the space DRE, $DU_{t\,x,y}$, is defined by

$$DU_{x,y}(x,y)= \frac{1}{T}\int\{u_{in}(x,y,t)-u_{rec}(x,y,t)\}dt \quad (2)$$

b) The overall performance evaluation is based on comparisons (b.i) of the radial velocity components from the HF-radar derived fields versus those from the actual drifters, and (b.ii) between the tracks and velocities of real versus virtual drifters deployed within the radar coverage area.

In order to evaluate the radar performance as well as the quality of the reconstructed data via the (b.i) approach, we compared the radial velocities of drifters with the radial velocities of the original HF radar data as well as of the reconstructed data.

The differences are quantified in terms of bias error and RMS error, where bias error b is $b=\langle udiff\rangle$ and RMS error is $RSM=\sqrt{\langle\left(udiff^{2}\right)\rangle}$ where $u_{diff}= u_{radar}-u_{drifter}$ averaged over time, the $<\,>$ symbols denote averaging, $u_{radar}$ the radar-derived radial velocity and $u_{drifter}$ the radial component of the velocity obtained from the drifter track (Molcard *et al.,* 2009). The (bii) comparison provides an overall evaluation of the final HF-radar derived velocity fields.

In order to proceed to the (b.ii) comparison, virtual drifter tracks (Mantovanelli *et al.,* 2011) were calculated by temporal integration of the radar-recorded velocities, initialized at the actual CODE-type drifter deployment positions (in time and space) during the aforementioned MedEX and TOSCA experiments. Numerical integration is performed using a fourth-order Runge-Kutta method for the time integration with a time step of 30 min combined with spatial interpolation on the u, v components of the radar-derived velocity fields. The trajectories comparison was applied to all the drifters deployed in the framework of the MedEX and TOSCA experiments. The comparison is performed by computing the separation distance (*or deviation*) d between the real and the synthetic trajectories, as described by Molcard *et al.* (2009):

$$d(t)= r_{real}(t)-r_{virtual}(t) \quad (3)$$

where $r_{real}(t)$ and $r_{vitrual}(t)$ are the positions of the real and virtual drifters, respectively, at time *t*. In order to obtain an estimate of the relative error, the deviation *d* can be compared to the real displacement *D(t)* of drifters given by

$$D(t)= r_{real}(t)-r_{virtual}(t=0) \quad (4)$$

Finally, in order to assess which part of the deviation, or separation distance, *d*, can be attributed to sub-grid scale flow structures (Kaplan *et al.,* 2005), estimates of the dispersion at sub-grid scales, obtained through the deployment of clusters of drifters within the framework of the TOSCA experiments, provided the effective relative diffusivities following Manning & Churchill (2006):

$$K_e= \frac{d\sigma^2}{dt} \quad (5)$$

where $\sigma^2$ is the mean squared displacement of the drifters from the center of the cluster centroid. Temporal integration of (5) provides the evolution of the mean squared displacement, and from that we obtain a measure of the mean horizontal relative dispersion of the clusters:

$$\sigma(t)=\{\int_0^t K_e dt\}^{1/2} \quad (6)$$

## Results

### *Data coverage*

HF radar coverage is widely known to be sensitive to weather conditions, ionospheric reflection, sea-surface

758

*Medit. Mar. Sci., 15/4, 2014, SPECIAL ISSUE, 753-768*

conductivity as well as noise from interference (Gürgel *et al.*, 1999b). The range of the "Dardanos" installation has shown the expected sensitivity to weather conditions, exhibiting range reduction during calm conditions and during storms. An additional source of signal deterioration is the interference from an external source appearing only during daytime. The effect of this interference is reduced (but not totally eliminated) by frequency hopping, which works like this: before each acquisition a frequency scan takes place and the Tx is moved to the "cleanest" area of the allocated frequency band. Thus, due to the diurnal cycle of the interference, the radar's range often exhibits significant decay during daytime.

To evaluate radar coverage, the Mean Data Return (referring to the total vectors, and defined as the ratio of the number of "good" over "expected" observations for the whole period) is calculated for each pixel. Overall, the MDR of the original data record exhibits a strong radial gradient at a distance of about 45-50 km from the northern (Plaka) antenna site, thus reducing data availability in distant areas; about 45 km away from the antennas, MDR becomes less than 15% in the long term (Fig. 3a). Unfortunately, the region east of Imvros island, a site of confluence of the Dardanelles outflow with a southward current along the Saros Gulf coast, part of the Samothraki anticyclone (Olson *et al.,* 2007), is almost permanently shaded and our results only provide a crude estimation of the flow pattern there. It should also be noted that the original data

set exhibits a strong decay of the coverage off the SW of the island of Lemnos, due to the partial shading of the region by the coastal topography from the line-of-sight connecting the 'Plaka' antenna site to the north.

A question that might arise is whether the low salinity of the Dardanelles outflow could affect radar coverage. The Dardanelles outflow is characterized by surface low salinity waters (~30-32), that are rather cold in the winter (~12 °C). Thus, the lowest conductivity expected in the region of the Dardanelles outflow to the Aegean is about 3.5 mho/m. Based on the analysis by Gürgel *et al*. (1999c), range reduction due to the reduced salinity of the BSW is rather negligible: a conductivity of 0.7 mho/m results in a 50% reduction of radar coverage. Thus, in our case, the Dardanelles outflow does not significantly affect radar coverage.

### *Data reconstruction evaluation*

The results of the data reconstruction through the DINEOF method are presented in Figures 3b, 6 and 7. The MDR of the radar after the application of the method is presented in Figure 3b. Comparison with the spatial distribution of MDR prior to the DINEOF reconstruction reveals the great improvement in radar coverage provided by the method.

A comparison between the divergence (computed as $\theta u / \theta x + \theta v / \theta y$) of the initial and the reconstructed fields was performed and revealed good agreement. The reconstructed divergence fields were generally smoothed
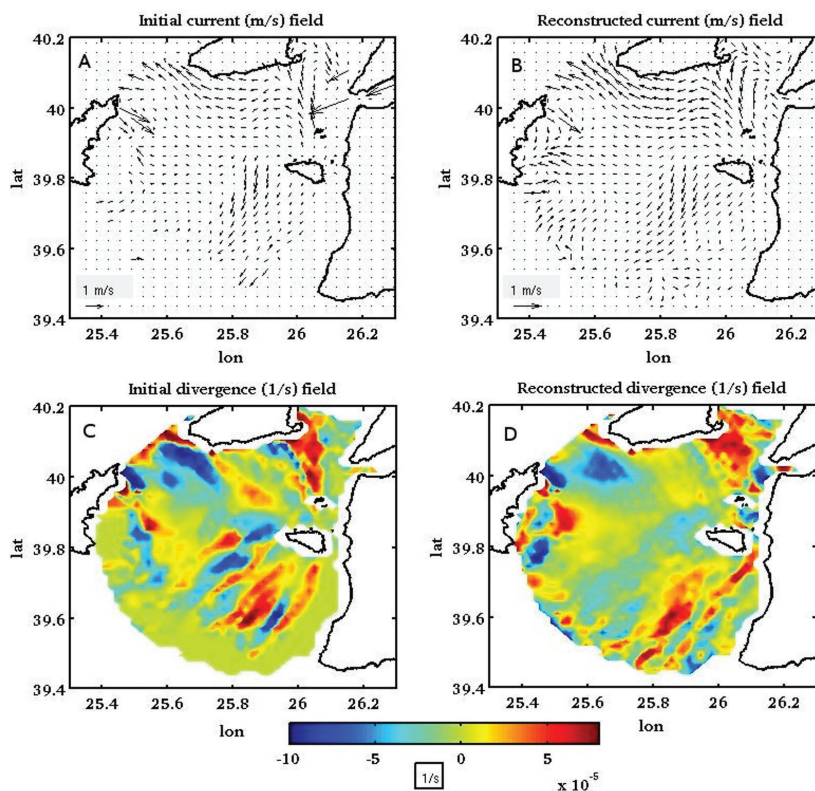


**Fig. 5:** Subfigures A and B present instantaneous current fields on Wednesday, Jan 20 2010 16:00-16:30. No value pixels are padded with zero. Subfigures C and D are the corresponding divergence fields.

compared to the initial ones (Fig. 5). By computing the divergence, we were also able to reveal the region of convergence along to the thermohaline front between Lemnos and Imvros islands (Fig. 5c, d).

The fidelity of the reconstructed velocity fields to the original fields is demonstrated by the metrics time ($DU_t$) and space ($DU_{x,y}$) Data Reconstruction Errors (RDE), defined by functions (1) and (2) respectively, and presented in Figures 6c and 6d as functions of time and space respectively, in comparison with the related distributions of mean data return (MDR). The $DU_t$ exhibits a mean value of less than 3cm/s; the largest values, more than 5cm/s (Fig. 6c), are observed when radar data return is less than 40% (Fig. 6a). A large part of this difference can be attributed to the variability of radar coverage, as the data return and $DU_t$ metrics exhibit a correlation coefficient of R=0.54. The space RDE, $DU_{x,y}$, of each pixel, along with its standard deviation, are presented in Figure 6d. The grid points are sorted according to their MDR (Fig. 6a),

and reveal the dependence of goodness of fit on the data return percentage. The mean difference is less than 5cm/s where MDR is larger than 30% and increases to about 10cm/s where MDR is less than 30%. On the other hand, standard deviations are generally less than 15cm/s where MDR is more than 50% and increase at low MDR values. It is noted that the MDR of a grid point never exceeded 65% for January 2010, partly due to technical problems, and partly due to partial spatial coverage of the scanned area.

The geographical distribution of the averaged speed difference between initial and reconstructed data is presented in Figure 7, exhibits four areas of larger differences, meaning low quality data, all of them located close to the boundaries of the coverage area. This is expected due to the Geometric Dilution of Precisions (GDOP), and for the radar coverage is provided by H. Messtechnik and is presented in Figure 8. The lower values of GDOP (<3.5) return better quality of data, the higher values (>3.5 &
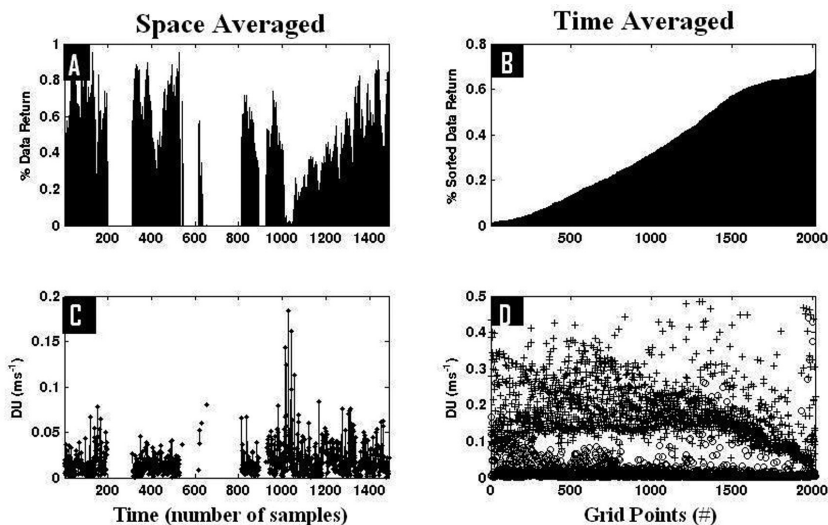


**Fig. 6:** A: Spatially averaged Mean Data Return as a function of time. B: Each pixel's time-averaged Data Return as a function of grid point, sorted in ascending order. C: $DU_t(t)$ as a function of time. D: $DU_{x,y}(x,y)$ mean values (o) and standard deviations (+) as a function of grid point, sorted in ascending mean data return values.
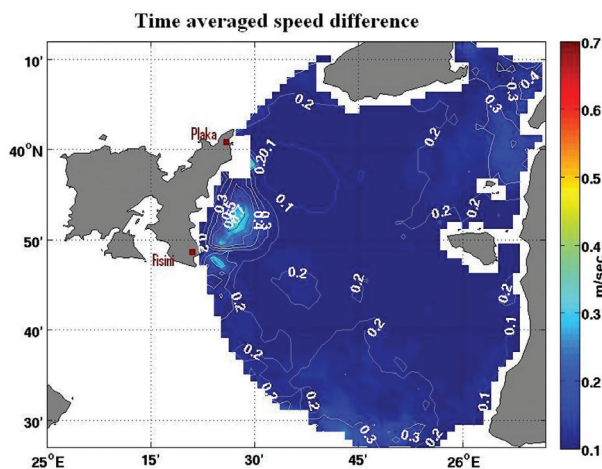


**Fig. 7:** Map of time averaged speed difference between initial and reconstructed data for January 2010.

<5) return lower quality of data, while areas with GDOP >5 are not considered as reliable radar coverage area. In front of the Plaka station there are essentially no data due to systematic errors caused probably by the area's anomalous topography. In front of the Dardanelles and in the southernmost part, the interpolation suffers, as data quality is reduced due to the proximity of angle-of-view to the two antenna sites, as well as the low MDR, especially at the Dardanelles entrance. However, it should be noted that the error should be reduced due to the stability of the direction of the flow along the Strait axis. Finally, in front of Fisini station, data return is sparse too; this should be attributed to the shaded line-of-sight to the Plaka station.

### *Evaluation of the overall performance of the HF-radar*

As mentioned above, the evaluation of the overall performance of the radar system is through ground-truthing, i.e. comparison to actual drifter information. The mean separation between HF-radar-derived, virtual drifter tracks and actual drifters tracks $d(t)$ is presented in Figure 9, compared to the actual drifter displacement $D(t)$, for both the TOSCA and MedEX experiments. Overlaid in Figure 9 is also the mean relative dispersion $\sigma(t)$ of a cluster of drifters, as derived by equation (6), based on TOSCA drifter cluster deployments.

Examination of Figure 9 reveals that overall more energetic conditions perseved during the TOSCA experiment, with the drifters covering a mean distance of about 6 km in 10 hours, in comparison with the MedEX experiments, where the corresponding mean distance covered would be about 3 km. The related mean separation of the HF-radar derived, virtual drifter tracks from
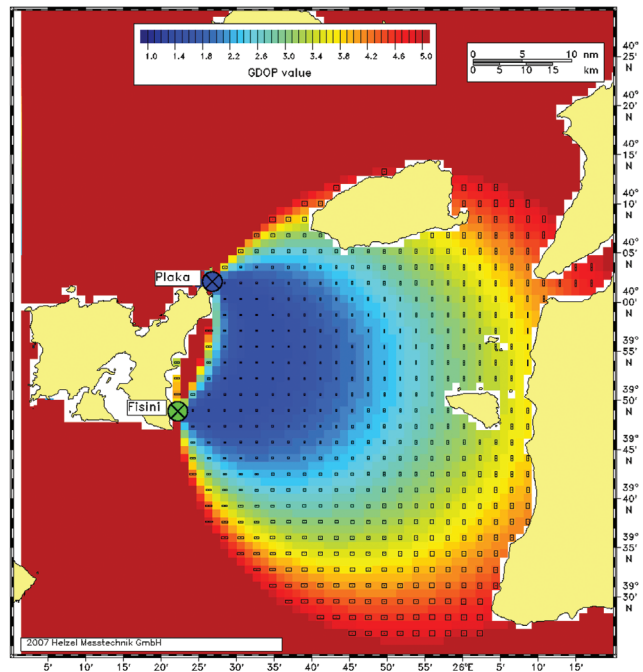


**Fig. 8:** Geometric Dilution of Precision (GDOP) map as provided by H. Messtechnik. Areas with values smaller than 5 are considered as acceptable.

the actual tracks in 10 hours would have increased to about 4 and 2 km respectively, values that represent a significant deviation between the virtual and the real drifter tracks. Figure 9 suggests that the ratio between the deviation and the distance covered by the drifters is between 50% and 70%. As a comparison, the mean drifter dispersion within a cluster remains very low, of the order of 200 m in ten hours. However, it should be noted here that
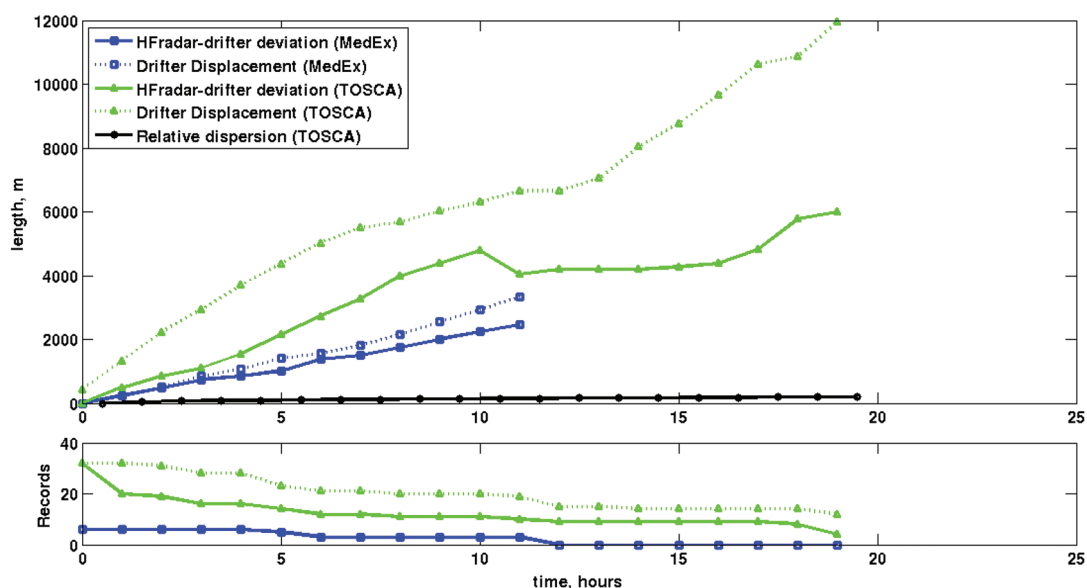


**Fig. 9:** Mean distance d(t) between actual and HF-radar-based, virtual drifters trajectories in all MedEx (in blue) and TOSCA (in green) experiments (upper panel). The mean drifter displacements D(t) (dashed lines) and the mean drifter-cluster dispersion σ(t) (thick black line) are also presented in the upper panel. The lower panel exhibits the number of drifter tracks employed in the calculations.

the mean separation estimate *d(t)* is biased towards high values by drifters deployed at poorly HF-radar covered regions, and that in well-covered HF-radar regions the virtual drifters tracks exhibited a much better agreement to the actual drifter tracks.

Another metric described above for the overall HF radar performance is the radial velocity differences between HF-radar measurements and drifter track measurements. This metric was applied on the two TOSCA experiments, in June 2012 and October 2012, when the mean quality of the radar data was bad and the coverage was sensitive to the existing external interference, especially during the day. The results of the comparison in terms of RMS and bias errors for the two experiments are presented in Table 2 below, both for the original, as well as the reconstructed data sets.

The $u_{diff} = u_{radar} - u_{drifter}$ values are presented in Figure 10, estimated for the reconstructed radar-derived fields. The maximum value of the radial velocity differences applied to the reconstructed data reaches 0.3 m/sec with the typical values being around 0.1 m/sec. These deviations are much higher in the original data set, a fact that shows the great improvement produced by the DINEOF data reconstruction. The differences between original and reconstructed radial velocities are significant and the comparison with the CODE type drifters shows a big improvement in the quality of the reconstructed data, despite the fact that the original data are limited and of bad quality. It is interesting to note the fact that in the region to the SE of Fisini, the radials to Plaka exhibit a much larger error than the ones at Fisini, which certifies that the bad quality of HF-radar data in this region is attributed to the poor coverage from the Plaka site due to marginal line-of-sight coverage.

## *Flow characteristics and variability*

The mean (calendar) seasonal surface velocity fields for 2010, as recorded by the "Dardanos" HF radar system, are presented in Figure 11. The mean velocity fields are

**Table 2.** Results of radial comparison between drifters and raw / reconstructed radar data.

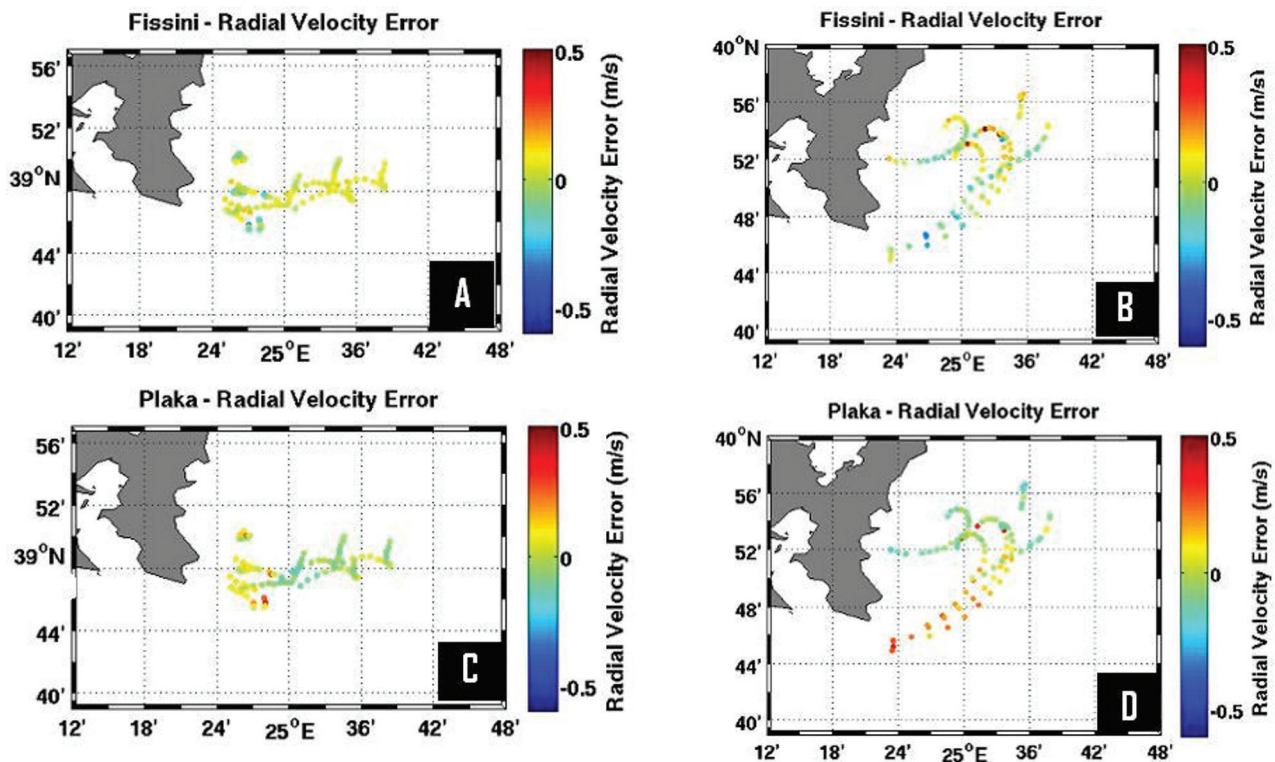| Parameter | Fisini (exp.1) | Plaka (exp.1) | Fisini (exp.2) | Plaka (exp.2) |
|---|---|---|---|---|
| Drifter radial velocity ( cm/sec) | 13 | 8 | 25 | 22 |
| **Raw:** Bias error (cm/sec) | -3 | 0 | 9 | 1 |
| **Reconstructed:** Bias error (cm/sec) | 0 | 1 | 2 | 3 |
| **Raw:** RMS Error (cm/sec) | 22 | 14 | 29 | 11 |
| **Reconstructed:** RMS Error (cm/sec) | 11 | 9 | 16 | 13 |



***Fig. 10:*** Values of reconstructed radial velocity differences ($U_{diff}$) along trajectories for Fisini, and Plaka Sites for the first experiment (left) and for the second (right).
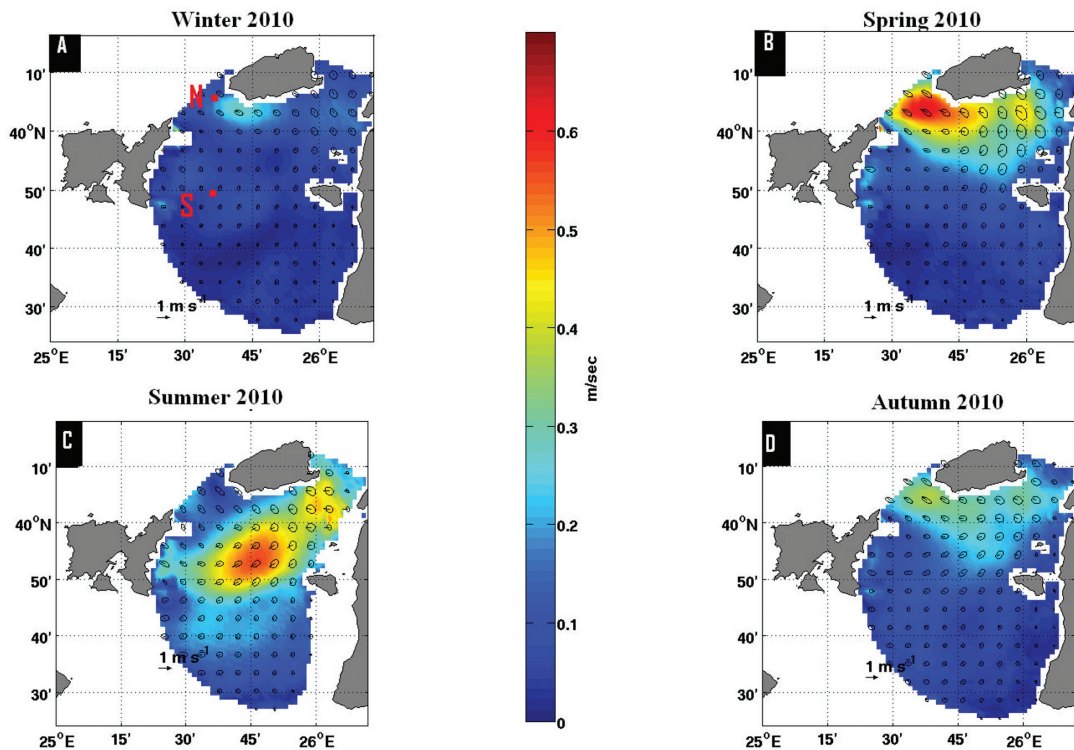
**Fig. 11:** Mean seasonal current velocity with variance ellipses of the current. In the top-left panel (the winter 2010 map), the positions of the selected points N and S are also identified (by red symbols).

displayed, with overlaid variance ellipses. The velocity maxima observed on the maps identify the presence of the Dardanelles outflow current, which exhibits significant seasonal variability: The current speed is high during spring (March-April-May) and summer (JJA), decreases during autumn (SON) and minimal values are recorded during winter (DJF). Furthermore, significant variability characterizes the seasonal mean current direction, as well as the position of the thermohaline front and the core of the BSW outflow. While during most of the year the current follows a westward track along the southern coast of Imvros island, during summer the flow detaches from the coast of Imvros and follows a southwestward track towards the southeastern cape of the island of Lemnos.

In order to obtain a better picture of the temporal variability of the flow, two positions located within the two different flow domains were selected (Fig. 10a, 11). The northern position, identified by the letter "N", is located within the main path of the Dardanelles outflow at the strait between the islands of Imvros and Lemnos (Fig. 10a). The southern position, identified by "S", is located in an area covered by Levantine waters most part of the year (Kourafalou & Barbopoulos, 2003), except during the late summer season when northerly winds, the *Etesians*, prevail (Poulos *et al.,* 1997; Savvidis, 2004; Tyrlis & Lelieveld*,* 2013). Furthermore, both positions are well covered by the HF radar. The temporal variability of the flow at the two points, "N" and "S", is presented in Figure 12.

In the northern area, the flow is dominated by a strong westward current that, at the "N" point location, turns west-northwestward, passing through the Strait between the islands of Imvros and Lemnos. The speed of the current often exceeds 0.5 m s$^{-1}$ during spring and autumn; however, it tends to be lower in the winter. Also, lower speeds are recorded during the late summer season, when the flow turns to southward dominant directions.

The southern domain of the HF radar coverage region is dominated by relatively weak currents of SW directions. The stability of the mean flow pattern is interrupted during March, when the flow is northward, and during the end of the year, when a weak north eastward flow is recorded. It is noteworthy that the flow in the southern region is intensified to exceed 0.5 m s$^{-1}$ only during the late summer season, when the flow at position "N" weakens and turns southward and the Dardanelles current appears to detach from the Imvros coast and turn to south-westward directions (Fig. 11).

In the Aegean Sea, upwelling occurs along the eastern shores of the sea due to the strong northerly winds (Etesians) that blows from mid-July until early September (Zodiatis *et al.,* 1996; Poulos et al., 1997). During these months (July and August 2010), in the southeast domain of the HF radar coverage, off the Asia Minor coast, we were able to identify west and northwest currents. These could represent the upwelling waters along the Turkish coast (Fig. 13).

An alternative way to examine the variability of the flow would be to look at the spatiotemporal variability of the four dominant EOF modes of surface circulation,
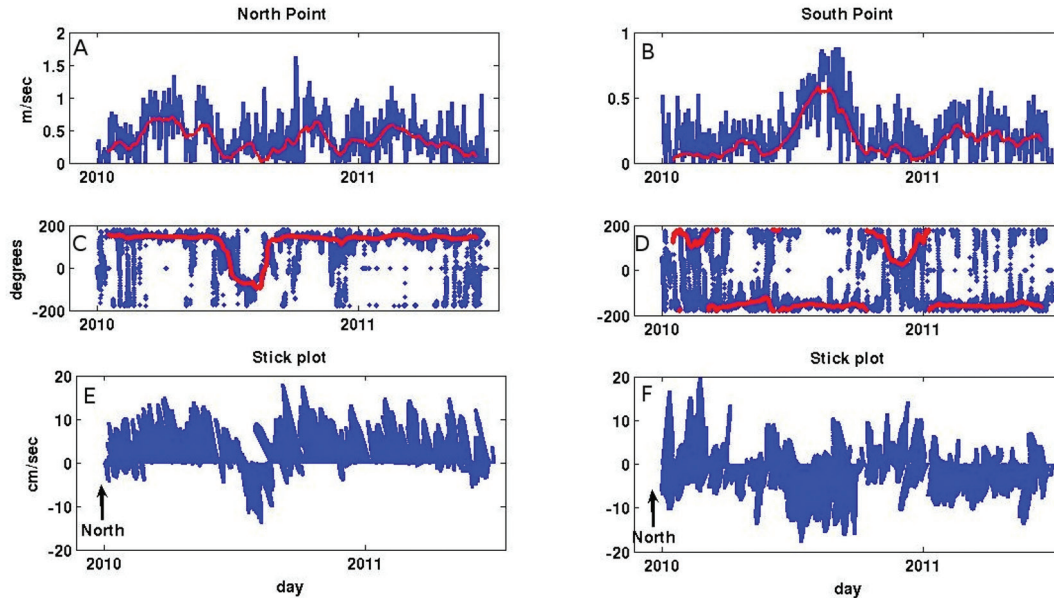
**Fig. 12:** Speed (A,B) , direction (C,D) and Stickplots (E,F) of the currents recorded at two representative positions for the flow, point N (left) and point S (right). The daily averaged values are presented in blue, monthly averages in red.
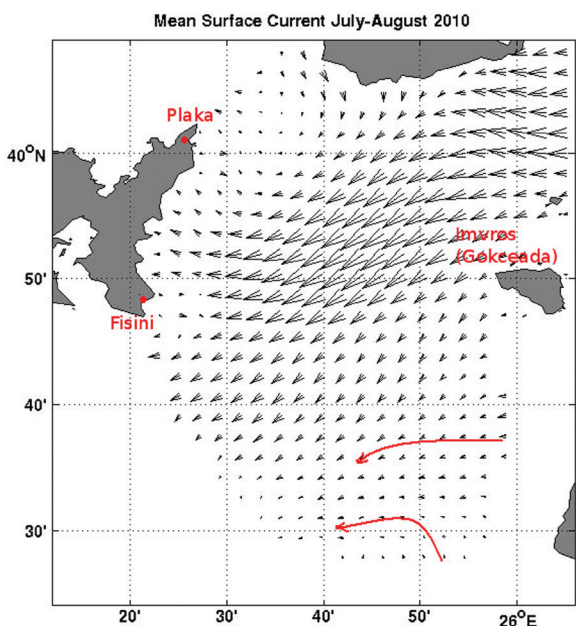


**Fig. 13:** Mean Surface current velocities for July-August 2010. One can observe the BSW traveling southwest, and also, the upwelled waters that travel west - northwest in the south region of radar coverage (red lines).

as revealed from the 2010 data record (Fig. 14b). These EOFs have not been calculated as described in the earlier section of the manuscript, as the objective here is not the high-resolution reconstruction of the data record, but the extraction of the dominant modes of circulation at larger spatiotemporal scales. Thus, in order to reduce the processing cost, the complete reconstructed data set has been temporally lowpassed and subsampled to daily values, and the resulting data set has been subjected to

EOF analysis. The total variance explained by the first four modes is 87%, and each of these in descending order, 57%, 13%, 6% and 4%. The four dominant EOF modes, responsible for the major part of the circulation, are presented in Figure 14 (spatial structure) and Figure 15 (temporal variability). It should be noted that the temporal variability coefficients of the EOF components are complex times series, thus contain information of magnitude and phase (angle). Thus, the ratio of the imaginary and real components determines the surface vector current rotation relative to the fields presented in Figure 14.

While the analysis of the dynamic response of the region to various forcing factors extends well beyond the subject, scope and length of this work, it is worthwhile to identify some major outcomes of EOF decomposition. Inspection of both the spatial and temporal variability of the modes suggests that the first three modes determine the major part of the seasonal evolution of the circulation. While mode 1, exhibiting the least divergence and curl of the flow, sets the largest scale of the north-south gradients and the annual Dardanelles discharge variability, mode 2 seems to control the most prominent seasonal variability feature, the change from the northern path to the southern path of the Dardanelles outflow current (Fig. 14, a,b). The spatial homogeneity of mode 1 also implies its dependence partly on the influence of the wind forcing, which is evident when examining its time evolution (Fig. 14, a). All four modes exhibit synoptic variability (Fig. 14). The second mode remains relatively unaffected by the synoptic variations as it contains the largest portion of energy at the annual and semiannual time scales. The fourth mode's convergence region at latitude 39° 45' is clearly associated with the thermohaline front created by Levantine and Black Sea waters of contrasting characteristics. Such an observation
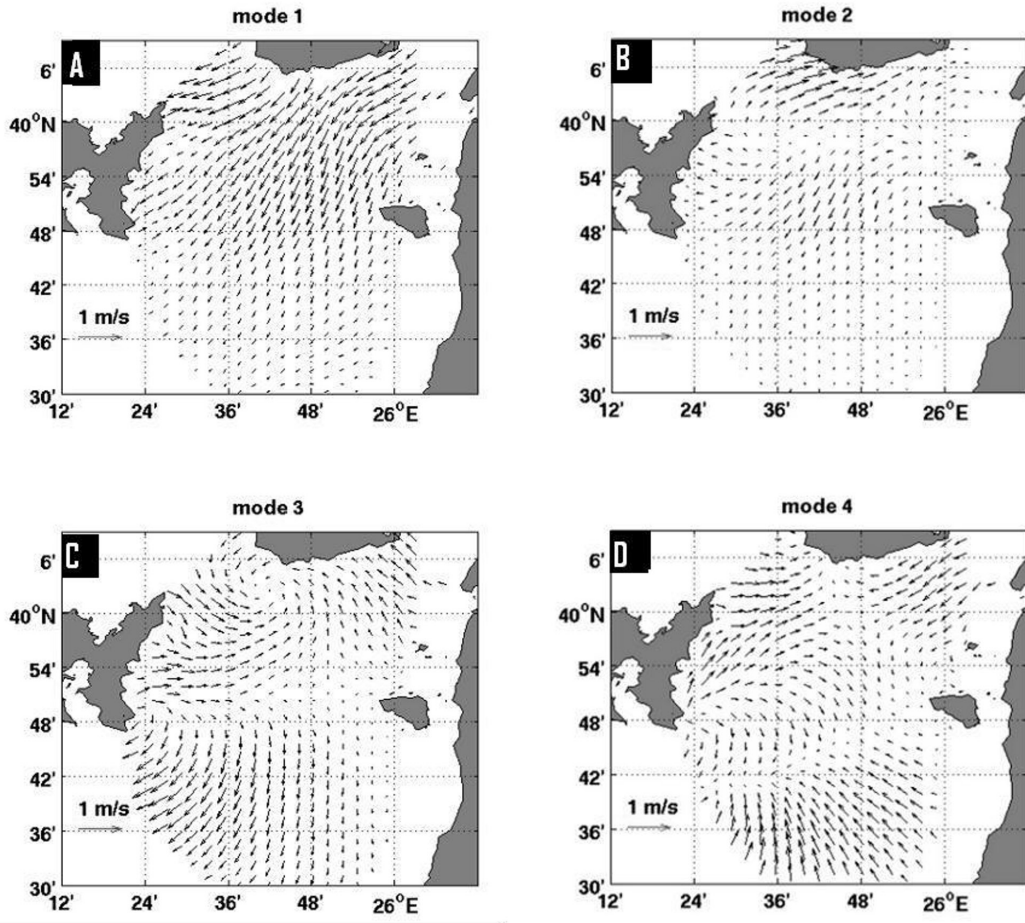
**Fig. 14:** The spatial structure of the four dominant EOF modes of the 2010 daily currents.
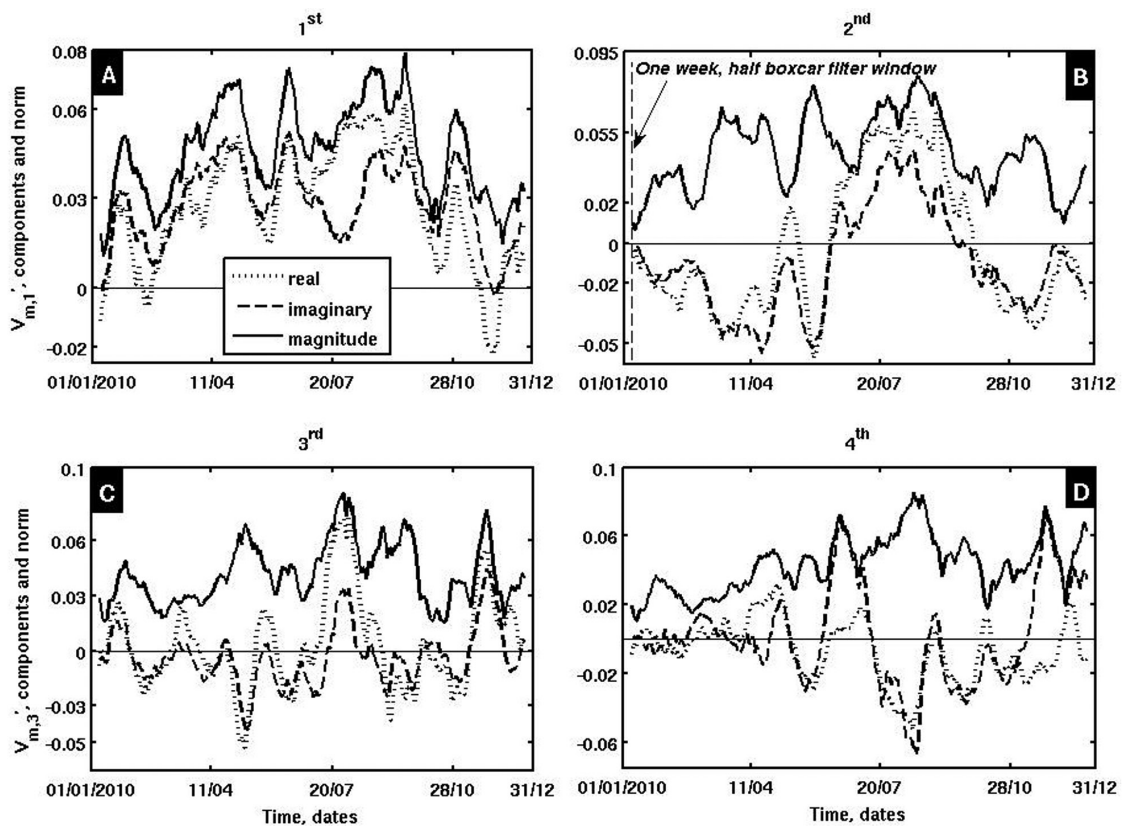


**Fig. 15:** Temporal structure of the four dominant modes of surface circulation.

suggests that during the alteration of the current from the northern to the southern path, the front region is a strongly convergent area. When the path alteration has been set, the front region is a divergent one, but with much smaller absolute values than the convergent phase. This may result from the movement of the front at lower latitude under the prolonged influence of the Etesians. It should also be noted that the fourth mode is the only one containing energy in the SE part of the coverage region (Fig. 14d) and also peaks in late summer (Fig. 15d), both facts suggesting that it is the major representative of the coastal upwelling process off the Turkish coast. Finally, the fourth mode (and partly the third mode) exhibits spatial scales comparable to the ones of the geomorphological features of the region, thus suggesting vorticity input from the interaction with the coast and probably the bottom relief

## Discussion

Globally, the main use of HF radars is real-time observation of coastal circulation and surface waves, which is especially useful for pollution management applications, Search-and-Rescue (S.A.R.) operations, and validation / assimilation purposes for model simulations. To our knowledge, the "Dardanos" installation is the first attempt globally to use HF radars mainly as a tool for climatic observations. To that effect, the radar covers a critical region of the Mediterranean – Black Sea exchange, monitoring the Dardanelles outflow surface current, which plays a major role both in the thermohaline overturning circulation of the Mediterranean and the functioning of the Aegean Sea ecosystem.

In order to achieve the above-described radar installation objectives, a complete, long and quality controlled time series of surface circulation maps of the region is required, overcoming inherent problems of HF radar technology, such as weather-depended and interference-sensitive coverage. In this work, we describe the development of a three-stage data-processing procedure, producing a quality controlled complete data-set that will constitute the start of a, hopefully, long time-series of the Mediterranean-Black Sea exchange.

The use of DINEOF for the development of a complete, quality-controlled record can be modified and applied at different stages of radar data preprocessing, which could possibly further improve the final product. The University of the Aegean group is currently working on further development such techniques, as well as investigating means for reducing external interference at the initial signal processing stage.

Another issue raised by the current work is the gradual separation of HF radar-derived and CODE-type drifter tracks. The results of trajectory comparisons were quite good, despite the fact that the radial velocity comparisons exhibit significant differences between radar and drifters. This is somewhat surprising, as the velocity error accu-

mulates through integration in the track calculation. This may be attributed to the short duration of the experiments due to the limited coverage of the radar and the fast motion of the drifters outside the area of interest. Longer experiments would probably result in greater differences between real and simulated tracks.

As mentioned in the manuscript, part of the separation arises from the discrepancy of the water volume sampled by the radar and by a CODE drifter: not only horizontally, where the point measurement of the drifter is compared with a grid scale average by the radar, but also vertically, where the vertical shear of the upper 1-m of the flow is averaged-out by the sail-design of a CODE drifter, while exponentially weighted by the HF radar (Stewart & Joy, 1974). Research work is underway at the University of the Aegean, Greece, and the Mediterranean Institute of Oceanography, France, to address this problem.

The seasonal evolution of the Dardanelles current, hereby revealed by the HF-radar measurements, agrees very well with previous analyses based on hydrographic measurements (Zodiatis & Balopoulos, 1993; Zodiatis, 1994; Zervakis & Georgopoulos 2002) as well as satellite observations (Skliris *et al.,* 2010). Furthermore, the strong velocity signal in spring may partly be related to the increased Dardanelles outflow during that period (Jarosz *et al.,* 2012, 2013; Vladimir Maderich, personal communication); however, the strong velocity signal during summer does not agree with the minimal Dardanelles outflow during that season. We suggest that the strength of the surface velocity signal is related to the stratification-maintained thermohaline contrast between the BSW and Levantine waters, as well as the directly wind-forced currents in the region. To verify this suggestion, correlation analysis between surface wind and radar-derived currents is underway.

The high spatial and temporal resolution of the HF system has revealed several features theoretically expected, but not observed in the past, such as the tendency of the Dardanelles current to flow along the south coast of Imvros and concentrate the inflow on the right of the flow through the Imvros-Lemnos Strait. The use of an HF radar gave us the opportunity to obtain higher resolution observations of the area and more systematic monitoring of that area. Another interesting feature is the weak southward flow at the above Strait during the late summer period under the influence of the Etesian winds. While satellite observation cannot shed much light on summer circulation due to the dominant signature of the upwelling (Skliris *et al.,* 2010), hydrographic observations suggest that during summer the Dardanelles outflow current bifurcates east of Lemnos to form two branches, one following a north-westward route through the Lemnos-Imvros strait and the other flowing to the southwest and around the south coast of Lemnos (Zervakis & Georgopoulos, 2002). The analysis of the radar-derived surface currents reveals a different picture, i.e. that the main

path of the Dardanelles current coincides with the southern branch, while the northern branch is not recorded. Interannual variability could explain part of the difference; however, we believe that the difference is largely due to the ageostrophic part of the circulation. While the vertical structure of the water column creates a sea-surface slope maintaining a north-westward geostrophic flow through the Strait, revealed through hydrographic measurements (Zervakis & Georgopoulos, 2002), the southward wind-forced currents during the Etesian period may exceed in amplitude and thus counterbalance the geostrophic flow, creating a weak southward surface flow at position "N" during these periods (as hereby suggested). Local direct measurements of current velocity during summer would shed light on this question.

Thus, the installation of an HF radar on the east coast of Lemnos island has introduced a tool that, with adequate processing and quality controlled procedures, could provide a long-term data series of the Mediterranean-Black Sea exchange, useful both for climatic and ecosystem studies and operational applications. Full exploitation of the system's capabilities will require a combination with information regarding the vertical structure of the water column and the velocity, as well as additional information from satellites. We believe that HF radars will prove to be useful instruments not only for operational applications but also for climatic studies, through the focused installation in Straits and significant climatic and ecosystem coastal areas, such as up-welling regions and deep-water formation sites.

## Acknowledgements

## References

Alvera-Azcárate, A., Barth, A., Sirjacobs, D., Beckers, J.-M., 2009. Enhancing temporal correlations in EOF expansions for the reconstruction of missing data using DINEOF. *Ocean Science*, 5, 475-485.

Alvera-Azcárate, A., Barth, A., Sirjacobs, D., Lenartz, F., Beckers, J.-M., 2011. Data Interpolating Empirical Orthogonal Functions (DINEOF): a tool for geophysical data analysis. *Mediterranean Marine Science*, 12 (3), 5-11.

Davis, R., 1985. Drifter observations of coastal surface currents during CODE: The method and descriptive view. *Journal of Geophysical Research*, 90, 4741-4755.

Emery, W.J., Thomson, R.E., 2004. The spatial analysis of data fields. p. 305-371. In: *Data Analysis Methods in Physical Oceanography*. Elsevier Science Inc (Ed.). Elsevier Publishers, Amsterdam.

Gertman, I.F., Pinardi, N., Popov, Y., Hecht, A., 2006. Aegean Sea water masses during the early stages of the Eastern Mediterranean Climatic Transient (1988–1990). *Journal of Physical Oceanography*, 36 (9), 1841-1859.

Gürgel, K.W., Antonischki, G., Essen, H.-H., Schlick, T., 1999a. Wellen Radar (WERA), a new ground-wave based HF radar for ocean remote sensing. *Coastal Engineering*, 37, (3-4), 219-234.

Gürgel, K.W., Essen, H.-H., Kingsley, S.P., 1999b. High-frequency radars: physical limitations and recent developments. *Coastal Engineering*, 37, (3-4), 201-218.

Gürgel, K.W., Essen, H.-H., Schlick, T., 1999c, p. 21-30. Applications of coastal radars for monitoring the coastal zone. *EUROMAR Workshop'99*, EUROMAR Office, Agência de Inovação, S.A., Av. dos Combatentes, 43, 10°C/D, 1600-042 Lisboa, Portugal.

Jarosz, E., Teague, W.J., Book, J.W., Beşiktepe, Ş.T., 2012. Observations on the characteristics of the exchange flow in the Dardanelles Strait. *Journal of Geophysical Research*, 117 (C11012), doi: 10.1029/2012JC008348.

Jarosz, E., Teague, W.J., Book, J.W., Beşiktepe, Ş.T., 2013. Observed volume fluxes and mixing in the Dardanelles Strait. *Journal of Geophysical Research*, 118, doi:10.1002/jgrc.20396.

Kaplan, D.M., Largier, J.L., Botsford, L.W., 2005. HF radar observations of surface circulation off Bodega Bay (northern California, USA). *Journal of Geophysical Research*, 110, C10020. doi:10.1029/2005JC002959.

Kelly, K.A., 1988. Comment on "Empirical orthogonal function analysis of advanced very high resolution radiometer surface temperature patterns in Santa Barbara Channel" by G.S.E. Lagerloef and R.L. Berstein. *Journal of Geophysical Research*, 93, 15753-15754.

Kourafalou, V.H., Barbopoulos, K.A., 2003. High resolution simulations on the North Aegean Sea seasonal circulation. *Annales Geophysicae*, 21, 511-265.

Lorenz, E., 1956. *Empirical orthogonal functions and statistical weather prediction*, Air Force Cambridge Research Center, Air Research and Development Command, Scientific Report, No. 1, 52 pp.

Lykousis, V., Chronis, G., Tselepides, A., Price, N.B., Theocharis, A. *et al.*, 2002. Major outputs of the recent multi-disciplinary biogeochemical researches undertaken in the Aegean Sea. *Journal of Marine Sciences*, 33-34, 313-334.

Malanotte-Rizzoli, P., Manca, B.B., Ribera d'Alcala, M., Theocharis, A., Bergamasco, A. *et al.*, 1997. A synthesis of the Ioni-

*Medit. Mar. Sci., 15/4, 2014, SPECIAL ISSUE, 753-768*

767

an Sea hydrography, circulation and water mass pathways during POEM-Phase I. *Progress in Oceanography*, 39, 153-204.

Manning, J.P., Churchill, J.H., 2006. Estimates of dispersion from clustered-drifter deployments on the southern flank of Georges Bank. *Deep Sea Research Part II*, 53, 23-24, 2501-2519.

Mantovanelli, A., Heron, M., Prytz, A., Steinberg, C.R., Wisdom, D., 2011. Validation of radar-based Lagrangian trajectories against surface-drogued drifters in the Coral Sea, Australia. *Oceans*, 11, 19-22.

Miller, A.R., 1963. Physical Oceanography of the Mediterranean Sea: a discourse. *Rapports et Proces-Verbaux des Reunions Commission Internationale pour l'Exploration Scientifique de la Mer Méditerranée*, 17 (3), 857-871.

Molcard, A., Poulain, P.M., Forget, P., Griffa, A., Barbin, Y. *et al*., 2009. Comparison between VHF radar observations and data from drifter clusters in the Gulf of La Spezia (Mediterranean Sea). *Journal of Marine Systems*, 78, 79-89.

Nielsen, J.N., 1912. Hydrography of the Mediterranean and adjacent waters. p. 72-192. In: *Report of the Danish Oceanographic Expedition 1908–1910 to the Mediterranean and Adjacent Waters*, *Volume 1*. Schmidt, J. (Ed.). Andr. Fred Høst & Søn, Copenhagen.

Olson, D., Kourafalou, V., Johns, W., Samuels, G., Veneziani, M., 2007. Aegean Surface Circulation from a Satellite-Tracked Drifter Array. *Journal of Physical Oceanography*, 37, 1898-1917.

Plakhin, Y.A., 1971. Formation of distinct deep water in the Mediterranean by convective mixing. *Oceanology*, 11 (4), 524-529.

Plakhin, Y.A., 1972. Vertical winter circulation in the Mediterranean. *Oceanology*, 12 (3), 344–351.

Pollak, M.I., 1951. The sources of deep water in the eastern Mediterranean Sea. *Journal of Marine Research*, 10, 128-152.

Poulos, S.E., Drakopoulos, P.G., Collins, M.B., 1997. Seasonal variability in sea-surface oceanographic conditions in the Aegean Sea (eastern Mediterranean): An overview. *Journal of Marine Systems*, 13, 225-244.

Roether, W., Manca, B.B., Klein, B., Bregant, D., Georgopoulos, D. *et al*., 1996. Recent changes in the Eastern Mediterranean deep waters. *Science*, 271, 333-335.

Roether, W., Klein B., Manca, B.B., Theocharis, A., Kioroglou, S., 2007. Transient Eastern Mediterranean deep waters in response to the massive dense-water output of the Aegean Sea in the 1990s. *Progress in Oceanography*, 74, 540-571.

Savvidis, Y.G., 2004. Modeling of the upwelling hydrodynamics in the Aegean Sea. *Mediterranean Marine Science*, 5 (1), 5-18.

Schlitzer, R., Roether, W., Oster, H., Junghans, H., Hausmann, M. *et al*., 1991. Chlorofluoromenthane and oxygen in the Eastern Mediterranean. *Deep-Sea Research*, 38, 1531- 1551.

Siokou-Frangou, I., Bianchi, M., Christaki, U., Christou, E.D., Giannakourou, A. *et al*., 2002. Carbon flow in the planktonic food web along a gradient of oligotrophy in the Aegean Sea (Mediterranean Sea). *Journal of Marine Systems*, 33-34, 335-353.

Skliris, N., Mantziafou, A., Sofianos, S., Gkanasos, A., 2010. Satellite-derived variability of the Aegean-Sea ecohydro-

dynamics. *Continental Shelf Research*, 30, 403-418.

Stewart, R.H., Joy, J.W., 1974. HF radio measurements of surface currents. *Deep-Sea Research*, 21, 1039-1049.

Sverdrup, H.U., Johnson, M.W., Fleming, R.H., 1947. Observations and collections at Sea. p. 331-388. In: *The Oceans: Their Physics, Chemistry and General Biology*. Stoddart, D.R., Johannes, R. (Eds), Prentice-Hall: Englewood Cliffs, NJ, USA.

Tolmazin, D., 1985. Changing coastal oceanography of the Black Sea. I. Northwestern Shelf. *Progress in Oceanography*, 15, 217-276.

Trujillo, D.A., Kelly, F.J., Perez, J.C., Riddles, H.R., Bonner, J.S., 2004. Accuracy of surface current velocity measurements obtained from HF radar in Corpus Christi Bay, Texas. Vol. 2, p. 1179-1182. In: *IEEE/ IGARSS Geoscience and Remote Sensing Symposium, Anchorage Alaska, 20 -24 September 2004*.

Tyrlis, E., Lelieveld, J., 2013. Climatology and Dynamics of the Summer Etesian Winds over the Eastern Mediterranean. Journal of the Atmospheric Sciences, 70 (11), 3374-3396.

Tzali, M., Sofianos, S., Mantziafou, A., Skliris, N., 2010. Modelling the impact of Black Sea water inflow on the North Aegean Sea hydrodynamics. *Ocean Dynamics*, 60, 585-596.

Ünlüata, U., Oguz, T., Latif, M.A., Ozsoy, E., 1990. On the Physical Oceanography of the Turkish Straits. p. 5-60. In: *The Physical Oceanography of Sea Straits*. NATO/ASI Series. Pratt, J. (Ed.). Kluwer Academic Publisher, Dordrecht.

Wüst, G., 1961. On the vertical circulation of the Mediterranean Sea. *Journal of Geophysical Research*, 66 (10), 3261-3271.

Zervakis, V., Georgopoulos, D., 2002. Hydrology and circulation in the North Aegean (Eastern Mediterranean) throughout 1997-1998. *Mediterranean Marine Science*, 3 (1), 5-20.

Zervakis, V., Georgopoulos, D., Drakopoulos, P.G., 2000. The role of the North Aegean in triggering the recent Eastern Mediterranean climatic changes. *Journal of Geophysical Research*, 105 (C11), 26103-26116.

Zervakis, V., Kalampokis, A., Kakagiannis, G., Georgakarakos, S., Saridakis, J., 2009. Low-cost drifters for coastal use. p. 333-337. In: *9th Hellenic Symposium of Oceanography and Fisheries*, Patras, 13-16 May 2009, HCMR, Athens.

Zervakis, V., Korres, G., Kokkini, Z., Tragou, E., Karambas, T., 2011. DARDANOS: A WERA system for monitoring the Dardanelles outflow in the Aegean. *Rapports de la Commission Internationale pour l'Exploration Scientifique de la Mer Méditerranée*, 39, 201.

Zodiatis, G., 1994. Advection of the Black Sea water in the north Aegean Sea. *Global Atmosphere and Ocean System*, 2, 41-60.

Zodiatis, G., Balopoulos, E., 1993. Structure and characteristics of fronts in the North Aegean Sea. *Bolletino di Oceanologia Theorica et Applicata*, 11, 113-124.

Zodiatis,G., Alexandri, S., Pavlakis, P., Jonsson, L., Kallos. G. *et al*., 1996. Tentative study of flow patterns in the North Aegean Sea using NOAA-AVHRR images and 2D model simulation. *Annales Geophysicae*, 14, 1221-1231.

768

*Medit. Mar. Sci., 15/4, 2014, SPECIAL ISSUE, 753-768*